P. Diehl, R. Lipton, M. A. Schweitzer

Numerical verification of a bond-based softening peridynamic model for small displacements: Deducing material parameters from classical linear theory

Abstract

In this article we present a systematic numerical approach for calibration and numerical verification of peridynamics models. The approach is illustrated for a two parameter exponential bond softening model, which is calibrated using theoretical relations connecting its horizon-independent parameters to the shear modulus and fracture toughness of classic Linear Elastic Fracture Mechanics. The horizon is determined by Griffith's brittle failure criterion given in terms of the critical failure stress which can be found experimentally. Computations with the calibrated peridynamic model are carried out to verify the linear behavior of the deformation for small strains and the Poisson effect. Numerical experiments identical to physical experiments are used to compute the Poisson ratio from samples subjected to linear time-dependent loading. The ratio observed in the experimental tensile test was reproduced in the simulations but becomes unstable after some time steps. We conclude that one explanation for this discrepancy that the simple peridynamic model has a peridynamically equivalent Poisson ratio of $1/4$ and the Poisson ratio of PMMA is 0.4. Our numerical results indicate that state-based peridynamics models with peridynamically equivalent Poisson ratios of 0.4 should be considered for a more stable recovery of material behavior for PMMA. As future work the same energy equivalence and comparison of material behavior with respect to experiments for the state-based softening peridynamic model will be considered.

1   Introduction

The peridynamic formulation introduced in [15] and [19] is a non-local formulation of continuum mechanics expressed in terms of displacement differences as opposed to spatial derivatives of the displacement field. This feature provides the opportunity to simultaneously simulate kinematics involving both smooth displacements and defect evolution. Thus, peridynamic modeling provides a convenient computational method for evolving defects and fracture [1, 3, 5, 7, 18, 17, 20, 6]. However, verification of numerical simulations require a calibration of the peridynamic model to the physical properties of the material. In this article we present one systematic approach for calibrating and numerically verifying peridynamic models. We provide a means to identify regimes where the numerical method recovers both experimentally determined and theoretically predicted values of the elastic moduli. The approach is illustrated for a specific two parameter exponential bond softening model. Where the model parameters are calibrated with the shear modulus and energy release rate. For this model the modeling parameters are independent on the horizon. Here the horizon is determined by Griffith's failure criteria. The critical stress to to cause brittle failure is obtained by a tensile test and the flaw size is deduced from Griffith failure criteria. Thus, the nodal spacing in the discrete model is left as a parameter which is not given by Linear Elastic Fracture Mechanics or experiments. This parameter can be obtained by the so-called m-convergence [2]. These are simple examples motivated by the family of bond softening models presented in [11, 10], which are known to recover sharp crack evolution having bounded Griffith fracture energy and linear elastic wave propagation away from the crack as the length scale of non-local interaction goes to zero see, [11], and [10].

2   Bond-based softening peridynamics model

The bond softening model is a smooth version of the bond breaking model introduced in [15]. Instead of bond breaking we have bond softening and because of this it is shown that this model delivers a force - strain law derived from a two-well potential [11], and [10], see Figure 1. One well is centered at zero strain and is associated with elastic energy and the second is based at infinity and associated with surface energy. The strain is calculated as the difference quotient of displacements between two points x and y. The force between two points x and y is related to the strain through a nonlinear cohesive law that depends upon the magnitude and direction of the strain, see Figure 3. Forces are initially elastic for small strains and soften beyond a critical strain. The non-local interaction between x and its neighbors y occur within a horizon of radius δ about x and the characteristic length of the material domain $D \subset \mathbb{R}^3$ is taken to be unity. This neighborhood of x is the ball $B_\delta(x)$ of radius δ with center x.

To define the potential, we introduce the deformation z by $z(x) = u(x) + x$ where u is the displacement field. The general strain $\mathcal{S}$ between two points x and y inside D is given by

$$\mathcal{S}(x,y) = \frac{|z(y) - z(x)| - |y - x|}{|y - x|}. \tag{1}$$

In what follows, we will assume small deformation kinematics and the displacements are small (infinitesimal) relative to the size of the horizon δ. Under this hypothesis (1) is linearized and the linear strain is

$$\mathcal{S}(x,y) = \frac{u(y) - u(x)}{|y - x|} \cdot e, \text{ where } e = \frac{y - x}{|y - x|}. \tag{2}$$

For the ease of notation we drop the explicit depends of the strain $\mathcal{S}$ on x and y. The bond softening model is characterized through a non-local potential

$$W^\delta(\mathcal{S}, y - x)$$

associated with points x and y. The associated energy density is obtained by integrating over y for x fixed and is therefore given by

$$\mathbf{W}^\delta(\mathcal{S}, x) = \frac{1}{V_\delta} \int_{B_\delta(x)} W^\delta(\mathcal{S}, y - x) \, dy, \tag{3}$$

where $V_\delta = \delta^3 4\pi/3$ is the volume of $B_\delta(x)$. The potential energy of the body is given by

$$PD^\delta(u) = \int_D \mathbf{W}^\delta(\mathcal{S}(u), x) \, dx. \tag{4}$$

We now introduce a particular class of potentials $\mathcal{W}^\delta$ associated with a cohesive force that is initially elastic and
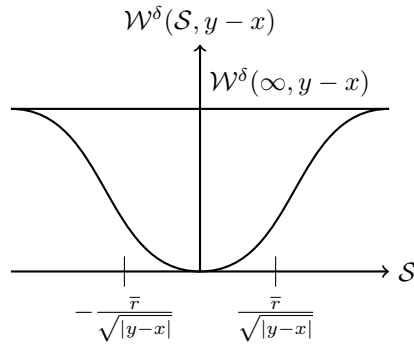

Figure 1: Potential as a function of $\mathcal{S}$ for x and y fixed. The well at zero corresponds to elastic energy, the well at ∞ corresponding to the horizontal asymptote corresponds with fracture energy.
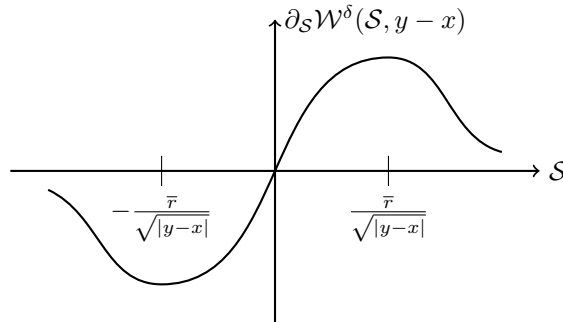

Figure 2: Relation between strain $\mathcal{S}$ and force $\partial_\mathcal{S} \mathcal{W}^\delta$ for fixed x and y for the bond softening model.

then softens after a critical strain. These potentials satisfy

$$W^\delta(\mathcal{S}, y - x) = |y - x|\mathcal{W}^\delta(\mathcal{S}, y - x), \tag{5}$$

where $\mathcal{W}^\delta(\mathcal{S}, y - x)$ is the peridynamic potential per unit length associated with x and y given by

$$\mathcal{W}^\delta(\mathcal{S}, y - x) = \frac{1}{\delta} J^\delta(|y - x|) \left(\frac{1}{|y - x|} f\left(|y - x|\mathcal{S}^2\right) \right). \tag{6}$$

These potentials are of a general form and are defined by potential functions $f : [0, \infty) \to \mathbb{R}$ that are positive, smooth and concave with the properties

$$\lim_{r \to 0^+} \frac{f(r)}{r} = f'(0) > 0, \qquad\qquad \lim_{r \to \infty} f(r) = f_\infty < \infty. \tag{7}$$

The composition of f with $|y - x|\mathcal{S}^2$ given by (6) delivers the convex-concave dependence of $\mathcal{W}^\delta(\mathcal{S}, y - x)$ on $\mathcal{S}$ for fixed values of x and y, see Figure 1. Note, that $J^\delta(|y - x|)$ is used in (6) to prescribe the influence of the separation length $|y - x|$ on the force between x and y inside $B_\delta(x)$. J^δ is defined by the rescaling $J^\delta(|y - x|) = J(|y - x|/\delta)$ where we require $0 \le J(|\xi|) < M$ for ξ in the unit ball $B_1(0)$ and $J = 0$ for $|\xi| > 1$. For fixed x and y the inflection point of the potential energy (6) with respect to the strain $\mathcal{S}$ is given by $\bar{r}/\sqrt{|y - x|}$, where $\bar{r}$ is the inflection point of the function $r :\to f(r^2)$, see Figure 1. This choice of potential delivers an initially elastic and then softening constitutive law for the force along the direction e given by

$$\partial_\mathcal{S} \mathcal{W}^\delta(\mathcal{S}, y - x) = \frac{2}{\delta} \left(J^\delta(|y - x|) f'\left(|y - x|\mathcal{S}^2\right) \mathcal{S} \right). \tag{8}$$

2

The force between points y and x begins to drop at the softening value where the strain $\mathcal{S}$ exceeds the critical strain

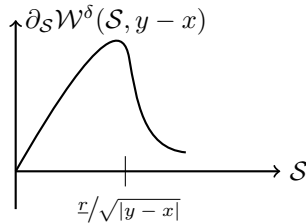$$|\mathcal{S}| > \frac{\overline{r}}{\sqrt{|y - x|}} =: \mathcal{S}_c, \tag{9}$$

see Figure 3.

Figure 3: Sketch of the force $\partial_{\mathcal{S}} \mathcal{W}^{\delta}(\mathcal{S}, y - x)$ for $|y - x|$ fixed.

The peridynamic equation of motion for the bond softening model is given by

$$\rho \partial_{tt}^2 u(t, x) = 2 \frac{1}{V_{\delta}} \int_{B_{\delta}(x)} \partial_{\mathcal{S}} \mathcal{W}^{\delta}(\mathcal{S}, y - x) \frac{y - x}{|y - x|} \, dy + b(t, x), \text{ for } x \in D, \tag{10}$$

where ρ is the material density and $b(t, x)$ is the external body force per unit volume. For the numerical results in Section 4 the equation of motion (10) is discretized with the so-called EMU nodal discretization [12]. Here, the body D is discretized with material points $X_i = (X_{i_1}, X_{i_2}, X_{i_3})$ at the discrete positions $X := \{X_1, \ldots, X_n \,|\, X_i \in \mathbb{R}^3\}$ with the associated surrounding volumes $V := \{V_1, \ldots, V_n \,|\, V_i \in \mathbb{R}\}$ (see Figure 4). Where we make the assumptions: $V_i \cap V_j = \emptyset$ and $\sum_{i=1}^n V_i \approx V_{\delta}$. The discrete neighborhood $B_{\delta}(X_i)$ of a material point at position X_i is given by $B_{\delta}(X_i) := \{j \,|\, |X_j - X_i| < \delta\}$. As a consequence the discrete version of the equation of motion for the bond-based softening model (10) for $X_i \in X$ is obtained as

$$\rho \partial_{tt}^2 u(t, X_i) = \frac{2}{V_{\delta}} \sum_{j \in B_{\delta}(X_i)} \partial_{\mathcal{S}} \mathcal{W}^{\delta}(\mathcal{S}, X_j - X_i) \frac{X_j - X_i}{|X_j - X_i|} V_j + b(t, X_i). \tag{11}$$
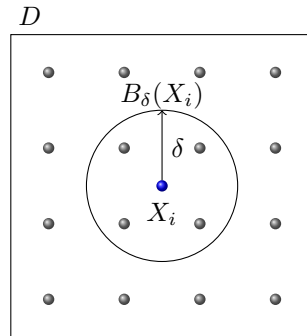

Figure 4: The material points at positions $\{X_i\}$ in the domain D in the reference configuration at time $t = 0$. For the material point at position X_i the neighborhood $B_{\delta}(X_i) := \{j \,|\, |X_j - X_i| < \delta\}$ is shown. The material point X_i exchanges pair-wise forces with all material points inside the neighborhood $B_{\delta}(X_i)$ through the so-called bonds.

2.1 Derivation of the peridynamic equivalent material parameters

This section introduces a peridynamic equivalent of the energy release rate G and the shear modulus μ from classical theory. First, the peridynamic equivalent energy release rate G_{PD} is addressed. The energy release rate is given by the energy per unit surface area required to eliminate force interaction between points on either side of a planar surface. In Figure 5 the peridynamic equivalent energy release rate G_{PD} (12) is calculated in terms of the energy $\mathcal{W}^{\delta}(\mathcal{S}, y - x)$ (6) per unit bond length $|y - x|$ necessary to completely soften all bonds ($\mathcal{S} \to \infty$) on either side of the fracture surface. To expedite the calculation we write $\zeta = x - y$ and the work to completely soften a bond is f_{∞}/δ. The energy release rate is given by the integral
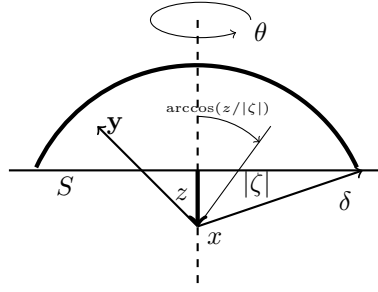
Figure 5: Evaluation of G_{PD}. For each point x along the dashed line, $0 \le z \le \delta$, the work required to break the interaction across the surface S between x and y in the spherical cap is summed up in (12) using spherical coordinates centered at x.

$$G_{\mathrm{PD}} = \frac{2}{V_\delta} \int\limits_0^\delta \int\limits_0^{2\pi} \int\limits_z^\delta \int\limits_0^{\arccos\left(\frac{z}{|\zeta|}\right)} J^\delta\left(|\zeta|\right) \frac{f_\infty}{\delta} |\zeta|^2 \sin\phi d\phi d|\zeta| d\theta dz \tag{12}$$

$$= \frac{6}{4} f_\infty \int\limits_0^1 J(r) r^3 dr,$$

see Figure 5. For this model the equivalent energy release rate is independent of the horizon δ.

Second, the peridyanmic equivalent shear modulus μ_{PD} is obtained. In classical theory the shear modulus μ describes the ratio of shear strain to shear stress. Here, the assumption is made that the strain (2) is small and the deformation is well approximated by a linear function at the length scale of the peridynamic interaction given by $u(x) = Mx$ where M is a symmetric 3×3 matrix. Then, the strain is given by

$$\mathcal{S} = M \frac{y - x}{||y - x||} \bullet \frac{y - x}{||y - x||} = \sum_{ij=1}^3 M_{ij} \frac{(y - x)_i}{(||y - x||} \frac{(y - x)_j}{||y - x||}. \tag{13}$$

Next, we expand the peridynamic potential per unit length (6) in a Taylor series in $|y - x|\mathcal{S}^2$ to second order to obtain

$$\mathcal{W}^\delta(y - x) \approx \frac{1}{\delta} \frac{f'(0)}{V_\delta} \int\limits_{B_\delta(x)} J^\delta(|y - x|)|y - x| \left(M \frac{|y - x|}{||y - x||} \bullet \frac{|y - x|}{||y - x||} \right)^2 dy. \tag{14}$$

Changing variables and rewriting the peridynamic potential (14) with respect to a unit ball $B_1(0)$ centered at the origin with volume denoted by ω_3 gives

$$\mathcal{W}^1(\xi) \approx \frac{f'(0)}{\omega_3} \int\limits_{B_1(0)} J(|\xi|)|\xi| \left(M \frac{\xi}{|\xi|} \bullet \frac{\xi}{|\xi|} \right)^2 d\xi \text{ with } \omega_3 = \frac{4}{3}\pi. \tag{15}$$

In addition, the approximated peridynamic potential (15) is transformed to polar coordinates and rewritten with respect to the tensor $\mathbb{C}_{\mathrm{PD}}$

$$\mathcal{W}^1(e) \approx \frac{f'(0)}{\omega_3} \int\limits_{B_1(0)} \int\limits_0^{2\pi} J(r) r^3 (Me \bullet e)^2 d\theta dr \tag{16}$$

$$\approx \sum_{i,j=1}^3 \sum_{k,l=1}^3 \left(\frac{f'(0)}{w_3} \int\limits_0^1 J(r) r^3 dr \right) \int\limits_0^{2\pi} e_i e_j e_k e_l d\theta D_{ij} D_{kl} \tag{17}$$

$$= \sum_{i,j,k,l=1}^3 \mathbb{C}_{\mathrm{PD}_{ijkl}} D_{ij} D_{kl}. \tag{18}$$

The tensor $\mathbb{C}_{\mathrm{PD}}$ is the peridynamic equivalent strain energy density for an isotropic elastic material. With Lemma 4.3 in [9] the isotropic tensor $\mathbb{C}_{ijkl}$ can be divided into the so-called bulk traces $\mathbb{C}_{iijj}$ and the so-called shear traces $\mathbb{C}_{ijij}$ where

$$\mathbb{C}_{iijj} = 3(2\mu + 3\lambda) \qquad \text{and} \qquad \mathbb{C}_{ijij} = 3(4\mu + \lambda). \tag{19}$$

4

Under the assumption, that $\mathcal{S}$ is small and linear with respect to the length scale of the horizon, we may also assume a behavior of the force per unit length $\partial_{\mathcal{S}}W^{\delta}(\mathcal{S}, |y - x|)$ so that the so-called shear trace $\mathbb{C}_{ijij}$ is equivalent to the peridynamic equivalent shear trace $\mathbb{C}_{\mathrm{PD}_{ijij}}$. Application of (19) then delivers the peridynamic equivalent shear modulus

$$\mu_{\mathrm{PD}} = \lambda_{PD} = \frac{f'(0)}{5} \int\limits_{0}^{1} J(r)r^3 dr, \tag{20}$$

where the equality of the moduli follows from the fact we have used a two point interaction potential and the peridynamic equivalent Poisson ratio is $\nu_{\mathrm{PD}} = 1/4$. Here the peridynamic horizon does not appear in the description of the peridynamic equivalent Young's modulus or Poisson ratio as these are local properties and correspond to the to $\delta = 0$ limit for this model. The peridynamic horizon also does not appear in the description of the energy release rate G_{PD} as the work per unit area required to eliminate interaction between two half planes is the same for all choices of delta, see (12).

To determine the horizon δ we employ the Griffith's fracture criterion for brittle materials. The critical stress for failure σ_{F} for a sample of brittle material is determined experimentally using a tensile test. The Griffith fracture criterion relates the critical stress to a flaw of size "a," and is given by

$$\sigma_{\mathrm{F}} = \sqrt{\frac{G_{\mathrm{PD}}E}{\pi a}} \tag{21}$$

or

$$a = \frac{G_{\mathrm{PD}}E}{\pi \sigma_{\mathrm{F}}^2}. \tag{22}$$

For fracture modeling the peridynamic horizon should be on a length scale small enough to resolve flaws of size "a." Direct calculation using this peridynamics model [10] shows that flaws given by a jump discontinuity in the displacement of length $a \geq \delta$ can become unstable and grow exponentially in time. Motivated by these two consderations we choose the horizon to satisfy $\delta \leq a$. Here we use the critical stress σ_{F} determined by a tensile test, see Figure 7(b), and Griffith's criterion as given by formula (22) is used to determine a.

2.2 Calibration of constitutive relations using classical theory

For our numerical investigation we use the two parameter exponential given by

$$f\left(|y - x|\mathcal{S}^2\right) = \beta\left(1 - e^{\left(-\alpha|y-x|\mathcal{S}^2\right)}\right), \tag{23}$$

where α and β denote the specific material parameters of this softening model. Figure 6(a) sketches this potential function f for varying parameters α and a fixed parameter $\beta = 1.5$. For $\mathcal{S} \to \infty$ the horizontal asymptote for this specific model yields $f(|y - x|\mathcal{S}^2) \to f_{\infty} = \beta$ and the first derivative $\partial f/\partial \mathcal{S}$ used in the force per unit length (8) is given by

$$\partial_{\mathcal{S}}W^{\delta} = \frac{J^{\delta}(|y - x|)}{\delta} \frac{2}{|y - x|} \frac{\partial f\left(|y - x|\mathcal{S}^2\right)}{\partial \mathcal{S}} = \alpha\beta \frac{J^{\delta}(|y - x|)}{\delta} e^{\left(-\alpha|y-x|\mathcal{S}^2\right)}\mathcal{S}. \tag{24}$$

Figure 6(b) sketches the variations of the derivative $\frac{\partial f}{\partial \mathcal{S}}$ of the potential function f with respect to the parameter α. Note that $f'(0) = \alpha\beta$ holds for all α and β.

More general bond force functions $f(r^2)$ allow for a more independent specification of linear elastic properties, strength and fracture toughness. The general twice differentiable bond force function of the form $f(r^2)$ is given in terms of a concave profile f expressed as

$$f(x) = f_{\infty}g(x) \tag{25}$$

with $g''(x) \leq$ on $0 \leq x \leq \bar{c}$, i.e., g concave, where we can take $\bar{c} = \infty$ and
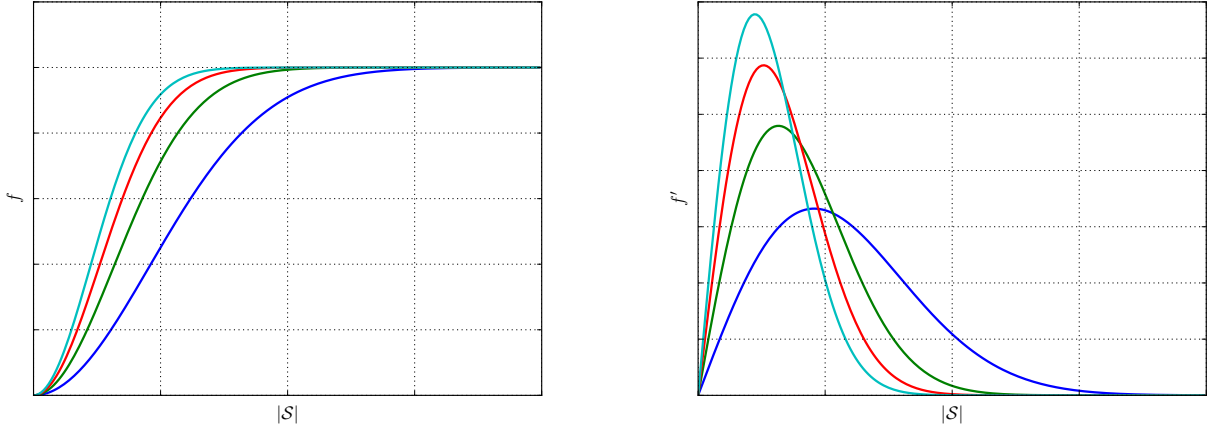
$$0 \leq g(x) \leq \min\{xg'(0), 1\} \tag{26}$$

with

$$g(0) = 0, g(\bar{c}) = 1, g'(\bar{c}) = 0, \text{ and } g''(\bar{c}) = 0. \tag{27}$$

Here the fracture toughness is determined as before from $f_{\infty} = \lim_{x \to \bar{c}} f(x)$, see (12), and the shear modulus from $f_{\infty}g'(0) = f'(0)$, see (20).

We can explicitly construct any potential function of the form $f(x) = f_{\infty}g(x)$ as follows. Pick any function $y(x) \leq 0$ defined on $0 \leq x \leq \bar{c}$ that satisfies $y(\bar{c}) = 0$ and

$$-\int_{0}^{\bar{c}} \tau y(\tau) d\tau = 1, \tag{28}$$

5

(a) Potential function f (23) for $|y-x|$ fixed and varying parameters α.

(b) Derivative f' for $|y-x|$ fixed and varying parameters α.

Figure 6: Variations of the material parameter α for the peridynamic potential function f (23) and its derivative f' (24).

then $g(x)$ satisfying properties (26), (27), with $g'' \leq 0$ is given by

$$g(x) = \int_0^x (x-\tau)y(\tau)\,d\tau - x\int_0^{\overline{c}} y(\tau)\,d\tau. \tag{29}$$

The two parameter exponential function (23) is a special case and follows on choosing $y(x) = -\alpha^2 e^{-\alpha x}$, $f_\infty = \beta$, and $\overline{c} = \infty$.

2.2.1 Calibration with shear modulus, energy release rate, and toughness

Next, we link the material parameters α and β to the shear modulus μ and the energy release rate G of classical LEFM via an energy equivalence. Table 1 shows the peridynamic equivalent shear modulus and energy release rate

Table 1: Peridynamic equivalent shear modulus μ_{PD} (20) and energy release rate G_{PD} (12) for the specific softening model with the corresponding potential function (23), i.e. $f'(0) = \alpha\beta$ and $f_\infty = \beta$.

Shear modulus	Energy release rate
$\mu_{\mathrm{PD}} = \dfrac{\alpha\beta}{5}\displaystyle\int_0^1 J(r)\,r^3 dr$	$G_{\mathrm{PD}} = \dfrac{6\beta}{4}\displaystyle\int_0^1 J(r)\,r^3 dr$

for the specific peridynamic potential with respect to the potential function (23) with $f_\infty = \beta$ and $f'(0) = \alpha\beta$. For the linear regime, before the bond starts to soften, the assumption is made that the peridynamic equivalent shear modulus μ_{PD} and energy release rate G_{PD} are equal to the shear modulus $\mu = {}^3/_5 K$ and the energy release rate $G = K_{\mathrm{Ic}}^2/E$ respectively. With these assumptions, the material parameters are dependent on the bulk modulus K and the critical stress intensity factor K_{Ic} and we obtain with $J(r) = 1$

$$\alpha = \frac{20\mu}{\beta} \qquad \text{and} \qquad \beta = \frac{16}{6}\frac{K_{\mathrm{Ic}}^2}{E}. \tag{30}$$

For the validation against classical theory in Section 4.2 the material parameters for Polymethylmethacrylate (PMMA) given in Table 2 are used to correlate the softening material parameters α and β to the parameters of the classical theory. For future reference we note that K is recovered from experimentally determined Young's modulus E and Poisson ratio using

$$K = E/(3(1-2\nu)).$$

The peridynamic horizon is determined by Griffith's failure criteria through (22). The failure stress is given by the maximum stress obtained from the stress versus strain curve obtained by tensile testing a sample of PMMA see Figure 7(b). Note, that for many other peridynamic models the horizon is an additional parameter and not related to any material property.
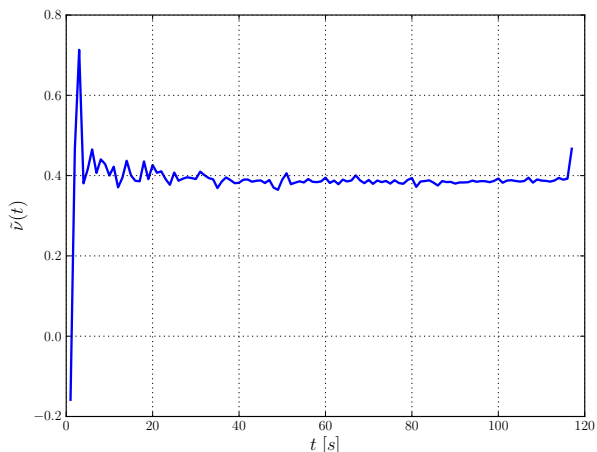
6

3 Model problem

A tensile test is a common way to experimentally recover elastic and strength properties from brittle materials. Here, the specimen of the observed material is placed at an electromechanical testing machine and a quasi-static load is applied. In addition, the experiment is observed with a stereo-microscope. These resulting pictures are applied with digital image correlation (DIC) to extract properties like the displacement, see Figure 13. These properties are used to compute the time-dependent Poisson ratio $\tilde{\nu}$. Figure 7(a) displays the Poisson ratio, obtained by the experiment, over time t until 120 seconds. At the beginning of the experiment the ratio is negative, shortly goes up to ≈ 0.7, shrinks to ≈ 0.4 and remains around this value until the specimen brakes. After 40 seconds the ratio lies in predicted range 0.4 which is common for PMMA material properties (Table 2). Figure 7(b) shows the global strain vs. stress curve determined by a tensile test and the failure strain σ_F is 52.8 MPa.

We address the following questions to validate the energy equivalence we applied in Section 2.2 to obtain the bond-based softening peridynamic material parameters:
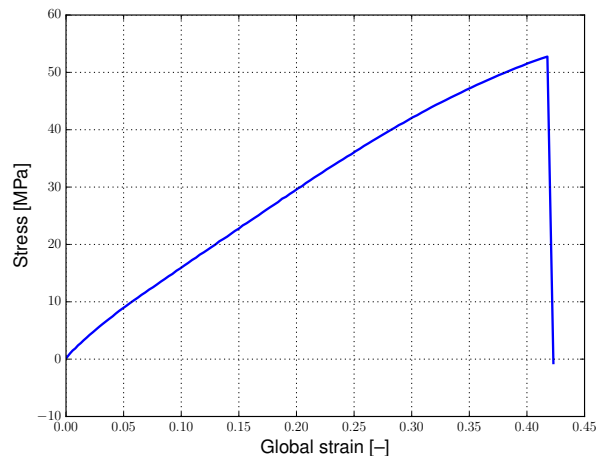
1. Can we reproduce the time-dependent behavior of the Poisson ratio like in the plot in Figure 7(a)?

2. Can we deduce the Poisson ratio of PMMA as prescribed in Table 2?

Table 2: Common material parameters for impact modified Polymethylmethacrylate (PMMA) with a composition (CH-C(CH3)COOCH3)n.

Material property	
Density ϱ	1.2×10^3 kg m^{-3}
Young modulus E	2.45 GPa
Poisson Ratio ν	0.4
Energy release rate G	500 Pa m
Shear modulus μ	1.7 GPa
Failure strain σ_F	52.8 MPa

(a) The time-dependent Poisson ratio for PMMA.

(b) The global strain vs. stress curve for PMMA.

Figure 7: The time-dependent Poisson ratio for PMMA (a) and global strain vs. stress curve 7(b) obtained by a experiment and extracted via digital image correlation (DIC).

3.1 Simulation setup

For all numerical simulations in Section 4 we consider a cubical domain D centered at $(1\,\text{m}, 1\,\text{m}, 1\,\text{m})^T$, compare Figure 8. The nodal spacing h of the nodes is obtained by the so-called m-convergence [2], such that the neighborhood $B_\delta(X_i)$ contains $2m+1$ nodes in $[X_i - \delta, X_i + \delta]$ in each direction. Thus, there a are $3 * (2 * m + 1) + 2$ nodes in each direction. We apply displacement in x-direction at the left and right boundary (green-colored nodes), i.e. $\pm 1\,\text{mm s}^{-1}$ which is a common value for an tensile test. In addition, we note that we had to wait for approximately 50 time steps until displacement could be obtained at the horizon in at the blue node. The central node (blue-colored node) located at $X_i = (1\text{m}, 1\text{m}, 1\text{m})^T$ and its neighborhood $B_\delta(X_i)$ is used in Section 4 for the numerical results for small

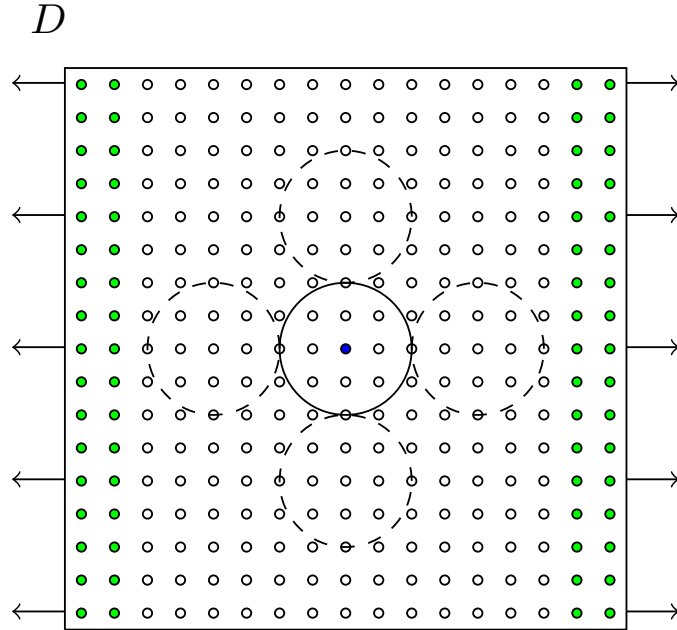Figure 8: Cross section in x-y-direction of the cube D centered at $(1\,\mathrm{m}, 1\,\mathrm{m}, 1\,\mathrm{m})^T$. The green colored nodes indicates where the displacement of $\pm 1\,\mathrm{mm\,s^{-1}}$ is applied.

deformations. First, in Section 4.1 we analyze the displacement field of the nodes inside the neighborhood $B_\delta(X_i)$. Here we check for the linearity of the displacement field in order to reproduce the elastic constants associated with the material. Second, the reproduction of the Poisson ratio ν (Section 4.2.1) is considered. The nodal spacing h of the nodes is obtained by the so-called m-convergence [2], such that the neighborhood $B_\delta(X_i)$ contains $2m+1$ nodes in $[X_i - \delta, X_i + \delta]$ in each direction. To avoid effects from surface correction or reflecting of waves in the numerical experiments additional neighborhoods (dashed ones) are located next to the neighborhood $B_\delta(X_i)$ as buffer zones. In the y-direction there are two additional layers at the top and bottom of the cube for symmetry. For the numerical experiments addressed in the next section we choose $m = [4, 13]$ thus for $m = 13$ we had 571787 nodes in the cube D, 9314 neighbors in side a full neighborhood B_δ, and a nodal spacing $h = 1.46 \times 10^{-5}\,\mathrm{m}$. The horizon $\delta = 0.00019\,\mathrm{m}$ is determined by Griffith's failure criteria (22), and a time step size $t = 1 \times 10^{-9}\,\mathrm{s}$ was chosen. Note, that the horizon and resulting nodal spacing is small, compared to the values used in many other publications. For this model we studied the m-convergence for a δ which is determined by experimental data. For asymptotically compatible discretizations in other contexts we refer to [4]. All simulations were performed on one Linux Fedora 25 node with Intel(R) Xeon(R) CPU E5-1650 v4 @ 3.60\,GHz, 32\,GB RAM, and running kernel version 4.8.10.

4 Numerical results for small deformations

4.1 Linearity of the displacement field

For this numerical experiment the displacement field of the nodes inside the neighborhood is considered. Due to symmetry of the displacement field, which was validated in the simulations, some nodes inside the neighborhood are not considered here. Figure 9 shows the nodes with these markers and colorization considered for study the displacement field. The nodes were selected according to

$$\begin{aligned}
\bullet &\Leftrightarrow \{X_j \mid X_j \in B_\delta(X_i) \wedge X_{j_1} = 1 \wedge X_{j_2} = 1\} \\
\triangle &\Leftrightarrow \{X_j \mid X_j \in B_\delta(X_i) \wedge X_{j_1} < 1 \wedge X_{j_2} > 1\} \\
\triangleright &\Leftrightarrow \{X_j \mid X_j \in B_\delta(X_i) \wedge X_{j_1} > 1 \wedge X_{j_2} < 1\},
\end{aligned} \tag{31}$$

such that all nodes $\bullet$ lie in the center of the interaction zone with respect to the x-y-plane. The other two types of nodes are chosen with respect to the octants of the three-dimensional coordinate system. We label the eight octants inside the neighborhood using a sign convention. The nodes $\triangle$ are in the octant $(-\ +\ +)$, the so-called top-back-right octant II and nodes $\triangleright$ are in the octant $(+\ -\ +)$, the so-called top-front-left octant IV, etc. For simplicity we use the respective roman numbers of the octants from now on. We address the following questions to validate the considered softening model:

1. Is the displacement linear for small bond stretches $\mathcal{S}$? The bond-based softening model and the energy equivalence with the classical theory (Section 2.2) is inferred under the assumption that the pair-wise bond

force (8) is in the linear regime before the bond starts to "soften" (Figure 6(b)). Therefore, the displacement has to be linear.

2. Is there no displacement at the node at X_i and very small displacement at nodes close to it? This point is in the center of the cube and since the boundary conditions are symmetric the node X_i should remain at rest.

3. Can we observe the so-called Poisson effect, i.e. a contraction of the material in the y-z plane due to the tensile loading in x-direction.
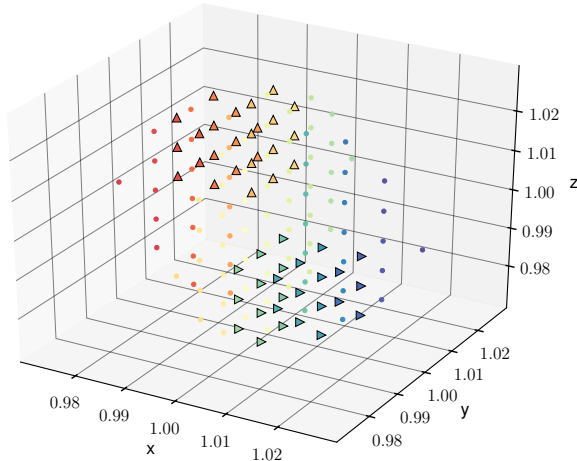

Figure 9: Nodes inside the neighborhood $B_\delta(X_i)$, such that the nodes $\bullet$ are in the center of the interaction $\{X_j \mid X_j \in B_\delta(X_i) \wedge X_{j_1} = 1 \wedge X_{j_2} = 1\}$, the nodes $\triangle$ are in the octant II $(-++)$, and the nodes $\triangleright$ in the octant IV $(+-+)$.

First, we focus on the linearity of the displacement field and Figure 10(a)-10(c) shows the plot of the displacement field in each direction (x, y, z) of the coordinate system for the selected nodes (31) inside the neighborhood $B_\delta(X_i)$. For all directions we see that until the normalized time step 0.3 there is no displacement for the nodes in $x-direction$ and up to 0.4 no displacement for the other two directions. Figure 10(a) shows the displacement in x-direction for the selected nodes inside the neighborhood. Note, that in this direction a displacement of $\pm 1 \, \text{mm s}^{-1}$ is applied.

For nodes $\triangle$ in octant II the displacement is negative in x-direction which agrees with the direction of the displacement $-1 \, \text{mm s}^{-1}$. Corresponding for the nodes $\triangleright$ in octant IV the displacement is positive which agrees with the direction of the displacement $+1 \, \text{mm s}^{-1}$. For the nodes $\bullet$ the displacement for nodes close to X_i is zero and for nodes very close at the boundary of the neighborhood $B_\delta(X_i)$ the displacement is in the lower range respective to the nodes in the corresponding octant. This behavior completely agrees with the applied external force and agrees with the material behavior of the pair-wise force (8). In addition, we see from plot of the strain versus force function in Figure 6(b) that the force strain relation is linear and the displacement remains linear for small strains s.

Figure 10(b) shows the displacement for the y-direction of the nodes inside the neighborhood. The nodes in octant II have a negative displacement which means the nodes move towards the center X_i and thus the length of the cube shrinks along the direction transverse to the applied force. For the nodes in octant IV the displacement is positive and the nodes move to the center X_i too. So here the length of the cube shrinks along the direction transverse to the force. Here, again the displacement at the node X_i and nodes are very close is zero and for nodes very close to the boundary of the neighborhood is in the lower range of the nodes in corresponding octants. The similarity to the linearity of the strain versus pair-wise force f and the linearity of the displacement field is seen as well.

Figure 10(c) shows the displacement in z-direction of the nodes inside the neighborhood. Because of symmetry of the material the displacement in z-direction of nodes in octant II and octant IV is similar to the displacement of the nodes in y-direction. The nodes in octant II have negative displacement and the nodes in octant IV have positive displacement. Thus, the length of the cube in z-direction shrinks too. Also, the displacement here is linear for small deformation.

Furthermore, the first question (*1.*) can be answered positive, because for small stretches s the displacement is linear in all three directions. So we can assume that for this simulation the force stays in the linear regime and therefore the assumptions we made in Section 2 hold. Hence, the definitions for obtaining the Poisson ratio ν and the Young modulus E for a linear elastic material in Section 4.2 are applicable.

Second, the displacement of the node $X_i = (1, 1, 1)^T$ and nodes very close to it are emphasized. The node X_i is in the center of the cube D. The displacement conditions applied at the green colored nodes in Figure 8 are symmetric with $\pm 1 \, \text{mm s}^{-1}$. As a consequence there is no displacement at this point, because the pair-wise force f is symmetric

and the pair-wise forces between the nodes X_i in the left of the neighborhood $\{X_j \mid X_j \in B_\delta(X_i) \wedge X_{j_1} < 1\}$ and the right of the neighborhood $\{X_j \mid X_j \in B_\delta(X_i) \wedge X_{j_2} > 1\}$ add up to zero (conservation of linear momentum). In Figures 10(a)-10(c) there is zero displacement at the node X_i and our simulation conserves the linear momentum.

Third, the so-called Poisson effect is studied. The Poisson effect, in our case the effect that a material expanded in one direction, tends to be shrinks in the respective other two directions. With the applied displacement conditions $\pm 1\,\mathrm{mm\,s^{-1}}$ in x-direction of the green colored layers in Figure 8 the cube is expanded in this direction. The negative displacement in octant II and the positive displacement in octant IV indicates that the cube is expanded in x-direction due to the applied force condition of the green colored layers. According to the Poisson effect the length of the cube in y-direction and z-direction should shrink. Looking at the displacement of the nodes in octant II and octant IV in these directions shows the Poisson effect. According to the Poisson effect the y-direction and z-direction is decreasing. This behavior is clearly observed for Figures 10(a)-10(c). The respective Poisson ratio obtained will be studied in the next section.

In addressing questions (*1.-3.*) we have shown that our simulation has a linear displacement field for small deformations. Thus, we stay in the linear regime and the validation with linear elastic theory in Section 4.2 is valid. In addition, we have shown that the considered bond-based softening model satisfies the conservation of linear momentum and reproduces the Poisson effect. These objectives indicate that our discretized version of the bond-based peridynamics softening model preserves the properties of the continuum model.

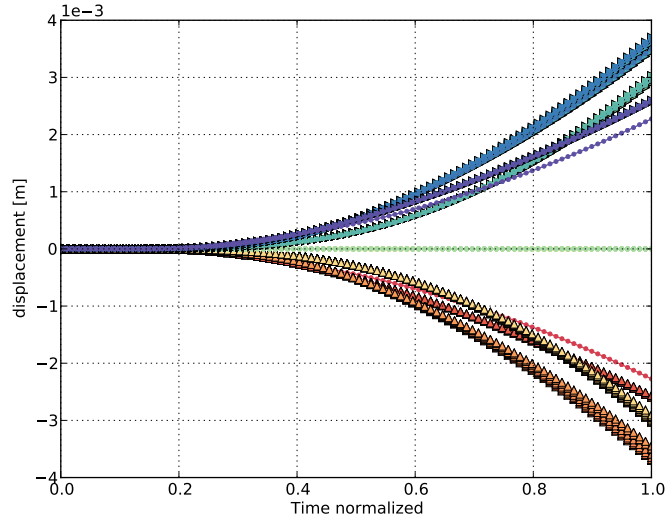## 4.2 Validation against experimental data

The Young modules E, the ratio of stress to strain and the Poisson ratio, the fraction of the expansion of the material divided by the compression for small changes; are two characteristic properties of a linear elastic material. For the validation with experimental data, we used the definition of the classical theory [13] for the Poisson ratio, see Equation (32). For the calculation of specific bond-based peridynamic softening model material parameters α and β in Section 2.2 the material properties of impact modified PMMA in Table 2 are used. Now, the discretized bond-based peridynamic softening model is used to estimate the Poisson ratio inside the neighborhood $B_\delta(X_i)$ (see Figure 11) via their definition from classical theory. Due to the energy equivalence we showed in Section 2.2 the simulations should reproduce the material parameters we used to calculate the bond-based peridynamic softening model material parameters α and β.

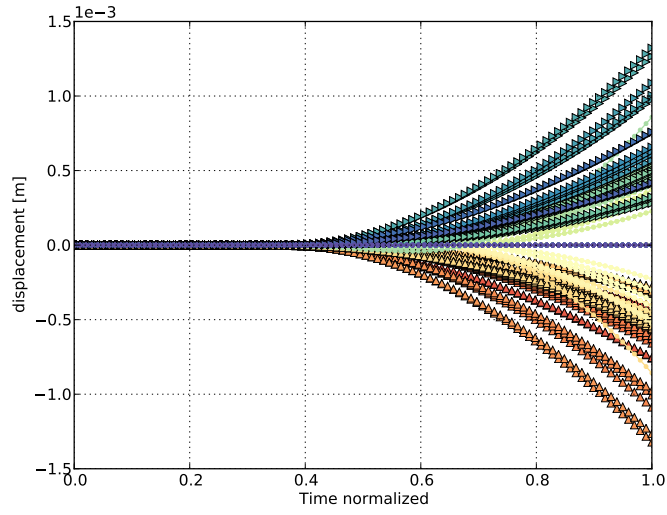### 4.2.1 Deduction of the Poisson ratio

In Section 4.1 the Poisson effect is observed in the displacement field of the nodes inside the neighborhood $B_\delta(X_i)$. Poisson ratio ν is a measurement for this effect and expresses the fraction of the expansion of the material divided by the compression for small length changes. In [14, 8] the Poisson ratio was obtained for the whole geometry. Our approach is novel in the way that we measure the Poisson ratio and the Young modulus directly inside in the neighborhood $B_\delta(X_i)$. Figure 11 sketches the neighborhood $B_\delta(X_i)$ of the node X_i centered at the mid of the cube. With $l_x(t)$, $l_y(t)$, and $l_z(t)$ we denote the length at time t respective the direction x, y, and z. Obviously the length in all directions at time $t = 0$ is 2δ. Equation (32) shows the time dependent definition of the Poisson ratio $\nu_y : [1, T] \to \mathbb{R}$, where the Poisson ratio ν by its definition from classical theory can be approximated for small changes of the length by

$$\nu_y(t) \approx -\frac{(l_y(t) - l_y(0))l_x(0)}{(l_x(t) - l_x(0))l_y(0)}$$
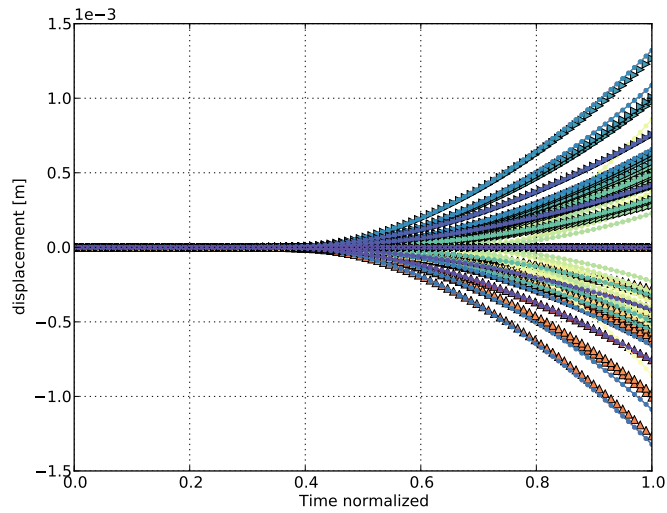$$\nu_z(t) \approx -\frac{(l_z(t) - l_z(0))l_x(0)}{(l_x(t) - l_x(0))l_z(0)}. \tag{32}$$

Note that a bond-based softening material model with a pair-wise force f is used in the simulation. Through the simplification that the force between two nodes X_i and X_j is independent of all other nodes inside the neighborhood $B_\delta(X_i)$, the Poisson ratio ν_{PD} is restricted to $1/4$ for a isotropic linear material. This restriction holds for molecular dynamics simulations with pair-wise potential too [16]. In [8] a extension for bond-based peridynamic material models for arbitrary Poisson ratios is presented. Our bond-based softening model is restricted to the peridynamically equivalent Poisson ratio $\nu_{\mathrm{PD}} = 1/4$. The common Poisson ratio for PMMA is $\nu_{\mathrm{PMMA}} = 0.4$, see Table 2. Figure 12 show the obtained Poisson ratio $v_{y_m}(t)$ inside the neighborhood $B_\delta(X_i)$ for $m = [4, 13]$, the dashed line refers to $\nu_{\mathrm{PMMA}} = 0.4$ and the dotted line refers to $\nu_{\mathrm{PD}} = 1/4$. For the time-dependent Poisson ratio we plotted for each m the first value where length change was obtained. The first obtained rate for all of them is 0.396, which is close to the one of PMMA. For all values of m the ratio the ratio stays for some time steps at this value. For m equals 7 and 9 the ratio drops after staying at 0.4 to 0.25 which is the peridynamically equivalent Poisson ratio $\nu_{\mathrm{PD}} = 1/4$. After some time steps all of the obtained rates decay to zero. Note, that the horizon and the nodal spacing in this model is quite small and thus the obtained displacement are small too. So the different behavior for m equals 7 and 9 could appear of fluctuation in the floating point operations. The behavior differs from the experiment in Figure 7(a).

(a) Displacement in x-direction of the nodes.

(b) Displacement in y-direction of the nodes.

(c) Displacement in z-direction of the nodes.

Figure 10: Displacement of the nodes inside the neighborhood $B_\delta(X_i)$
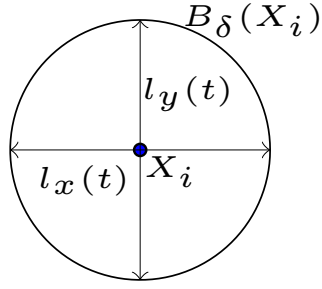
11

Figure 11: Sketch for obtaining the time dependent Poisson ratio $\nu_y(t)$ inside the interaction $B_\delta(X_i)$. Equation (32) shows the time dependent Poisson ratio $\nu_y : [1, T] \to \mathbb{R}$ with respect to the length change $l_x(t)$ and $l_y(t)$ over time t.
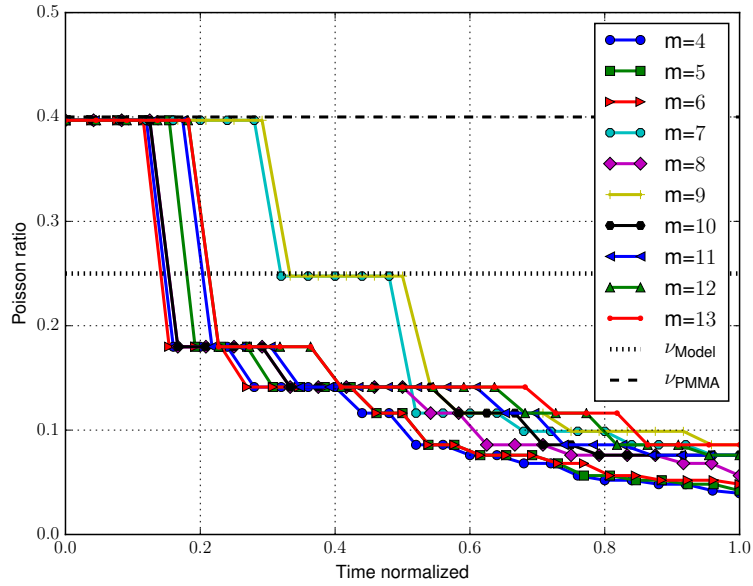

Figure 12: Time-dependent obtained Poisson ratio $\nu_{y_m}(t)$ in y-direction inside the neighborhood $B_\delta(X_i)$ for $m = [4, 13]$. The dotted line is the peridynamically equivalent Poisson ratio $\nu_{\mathrm{PD}} = 1/4$ and the dashed line is the Poisson ratio of the material $\nu_{\mathrm{PMMA}} = 0.4$. The obtained values $\nu_{z_m}(t)$ are identical for all m, because of symmetry of the Poisson ratio for an elastic isotropic material. For simplicity, we do not plot them here.

Here, there is a peak at the beginning and that the ratio diverges around 0.4 which is the Poisson ratio of PMMA. In the simulation we can not obtain this peak. We see that the obtained rate initially stays at 0.396, then drops to different values and decreases to zero. Note, that this behavior is independent of m for a fixed horizon $\delta = 0.00019$ which is determined by the experiment.

One reason for the different behavior of Poisson ratio $\nu(t)$ seen in the computational experiments portrayed in Figure 12 lies in the applied bond-based model. On the one hand this model is restricted to the peridynamic equivalent Poisson ratio $\nu_{\mathrm{PD}} = {}^1\!/_4$. On the other hand the Poison ratio of PMMA is $\nu_{\mathrm{PMMA}} = 0.4$. In addition, the obtained ratio in the experiment is measured in a larger area and compared to the horizon the measured area in the simulation is much smaller.

5   Conclusion

In this study we have calibrated a bond-based softening model and computationally verified it. The model is calibrated using the theoretical relations connecting the parameters of the two parameter exponential bond softening model to the shear modulus, energy release rate, and the peridynamc horizon to critical stress through Griffith's failure criterion. The two parameters of the exponential model depend on energy release rate and shear modulus and not on horizon. Here we use the m-convergence for $m = [4, 13]$ to determine the nodal spacing. Note, that in many other peridynamic model the horizon is a additional parameter to choose and not related to any material model. In our model the horizon is determined by the failure strain of the material which can be obtained in experiments like a tensile test. Recall, that the horizon and nodal spacing is small compared to the horizons used for other models in the literature.

Computations are carried out verifying the linear behavior of the deformation for small strains and Poisson effect. The verification for linear behavior is necessary due to the energy equivalence we used to determine the material parameters. The energy equivalence and the value of the failure strain are only valid for linear behavior. After this verification we then conduct numerical experiments identical to the physical experiments to compute at time-dependent Poisson ratio from samples subjected to linear time dependent loading. Here a material specimen of PMMA in the shape of a cube is loaded in uni-axial tension and subjected to an applied displacement. For all m the Poison ratio is close to the one of PMMA observed in the tensile test. In the experiment the ratio stays at 0.4 before dropping to zero when the specimen broke. In the simulations the ratio deceases after some time steps to different values before decreasing to zero. One explanation for the discrepancy is that the simple peridynamic model has a peridynamically equivalent Poisson ratio of ${}^1\!/_4$ and the Poisson ratio of PMMA is 0.4.

Our numerical results indicate that state-based peridynamics models with peridynamically equivalent Poisson ratios of 0.4 should be considered for a more stable recovery of material behavior for PMMA. As future work the same energy equivalence and comparison of material behavior with respect to experiments for the state-based softening peridynamic model will be considered.

A   Results from digital image correlation

Figure 13 shows one picture at the beginning of the experiment taken by the stereo-microscope. The specimen is mechanical prepared with the small black dots as markers for the digital image correlation (DIC). These markers are used with respect to reference configuration to extract quantity of interest, i.e. the displacement. With the displacement the Poisson's ratio like in Equation (32) is computed and plotted over time (see Figure 7(a)).

References

[1] Bobaru, F., and Hu, W. The meaning, selection, and use of the peridynamic horizon and its relation to crack branching in brittle materials. *International journal of fracture 176*, 2 (2012), 215 – 222.

[2] Bobaru, F., Yang, M., Alves, L. F., Silling, S. A., Askari, E., and Xu, J. Convergence, adaptive refinement, and scaling in 1d peridynamics. *International Journal for Numerical Methods in Engineering 77*, 6 (2009), 852–877.

[3] Dayal, K., and Bhattacharya, K. Kinetics of phase transformations in the peridynamic formulation of continuum mechanics. *Journal of the Mechanics and Physics of Solids 54*, 9 (2006), 1811–1842.

[4] Du, Q. *Handbook of Peridynamic Modeling*. CRC Press, September 2016, ch. Local Limits and Asymptotically Compatible Discretizations, pp. 89–110.

[5] Foster, J. T., Silling, S. A., and Chen, W. An energy based failure criterion for use with peridynamic states. *International Journal for Multiscale Computational Engineering 9*, 6 (2011).
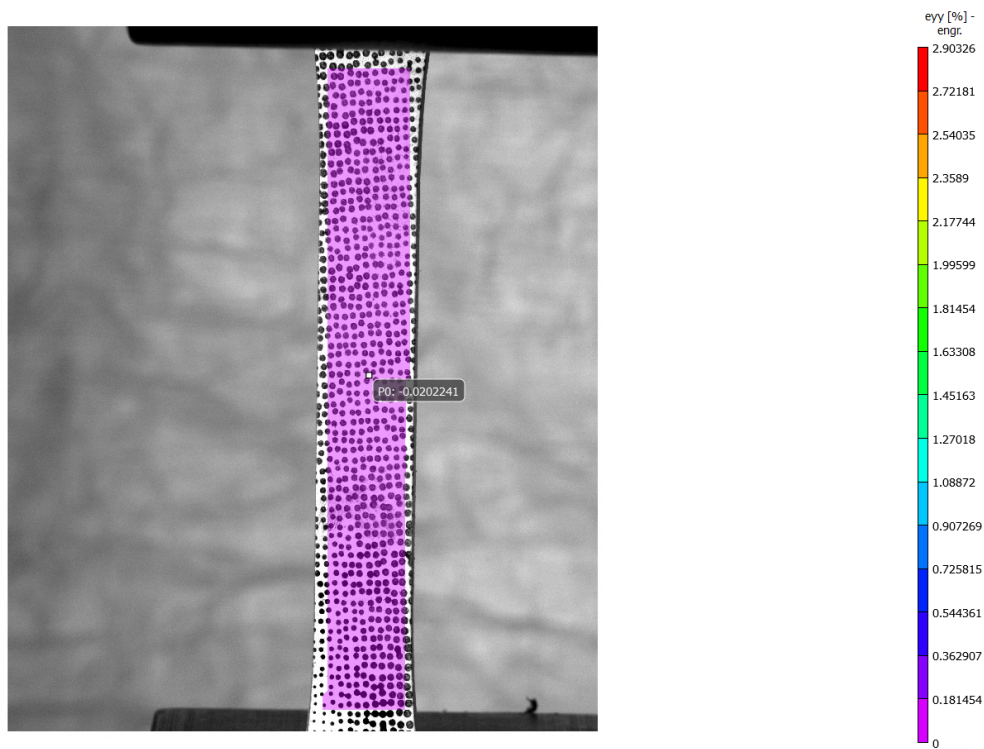
eyy [%] -
engr.

| 2.90326 |
| 2.72181 |
| 2.54035 |
| 2.3589 |
| 2.17744 |
| 1.99599 |
| 1.81454 |
| 1.63308 |
| 1.45163 |
| 1.27018 |
| 1.08872 |
| 0.907269 |
| 0.725815 |
| 0.544361 |
| 0.362907 |
| 0.181454 |
| 0 |

P0: -0.0202241

Figure 13: Extracted strain in y-direction of the experiment via digital image correlation

[6] GERSTLE, W., SAU, N., AND SILLING, S. Peridynamic modeling of concrete structures. *Nuclear engineering and design 237*, 12 (2007), 1250–1258.

[7] HA, Y. D., AND BOBARU, F. Studies of dynamic crack propagation and crack branching with peridynamics. *International Journal of Fracture 162*, 1-2 (2010), 229–244.

[8] HU, Y., AND MADENCI, E. Bond-based peridynamics with an arbitrary poissons ratio. In *57th AIAA/ASCE/AHS/ASC Structures, Structural Dynamics, and Materials Conference* (2016), p. 1722.

[9] JAMES, R., LIPTON, R., AND LUTOBORSKI, A. Laminar elastic composites with crystallographic symmetry. *SIAM Journal on Applied Mathematics 50*, 3 (1990), 683–702.

[10] LIPTON, R. Cohesive dynamics and brittle fracture. *Journal of Elasticity* (2015), 1–49.

[11] LIPTON, R. P. Dynamic brittle fracture as a small horizon limit of peridynamics. *Journal of Elasticity 117*, 1 (2014), 21–50.

[12] PARKS, M. L., LEHOUCQ, R. B., PLIMPTON, S. J., AND SILLING, S. A. Implementing peridynamics within a molecular dynamics code. *Computer Physics Communications 179*, 11 (2008), 777 – 783.

[13] ROYLANCE, D. Mechanical Properties of Materials. Lecutre Notes at the Massachusetts Institute of Technology, 2008.

[14] SAREGO, G., LE, Q. V., BOBARU, F., ZACCARIOTTO, M., AND GALVANETTO, U. Linearized state-based peridynamics for 2-d problems. *International Journal for Numerical Methods in Engineering* (2016).

[15] SILLING, S. Reformulation of elasticity theory for discontinuities and long-range forces. *Journal of the Mechanics and Physics of Solids 48*, 1 (2000), 175–209.

[16] SILLING, S. A. *Handbook of Peridynamic Modeling*. CRC Press, September 2016, ch. Introduction to Peridynamics, pp. 26–58.

[17] SILLING, S. A., AND ASKARI, E. A meshfree method based on the peridynamic model of solid mechanics. *Computers & structures 83*, 17 (2005), 1526–1535.

[18] SILLING, S. A., AND BOBARU, F. ”peridynamic modeling of membranes and fibers”. *International Journal of Non-Linear Mechanics 40*, 2 (2005), 395–409.

[19] SILLING, S. A., EPTON, M., WECKNER, O., XU, J., AND ASKARI, E. Peridynamic states and constitutive modeling. *Journal of Elasticity 88*, 2 (2007), 151–184.

[20] WECKNER, O., AND ABEYARATNE, R. The effect of long-range forces on the dynamics of a bar. *Journal of the Mechanics and Physics of Solids 53*, 3 (2005), 705–728.